

# A LIGHTCURVE EVALUATION FOR EXOPLANETARY SYSTEM HAT-P-23B (AST 443: LAB 1)

BRIANNA ISOLA (LAB PARTNERS: TYLER NILL, MATTHEW MURPHY)

## ABSTRACT

Observations of exoplanets that transit the disks of their host star can provide astronomers data that can characterize properties of the exoplanetary system. We present here a report one exoplanet transit observation and the subsequent analysis to characterize such properties. The exoplanet transit of HAT-P-23b was recorded with the the 14-inch Meade LX200-ACF telescope at the Mt. Stony Brook Observatory in Stony Brook, NY. Images were taken with an SBIG CCD camera and the data calibrated for the transit lightcurve. We find our equipment to be valid for our observation and present a distinct lightcurve plot with visual flux changes during transit. We take a numerical approach to analysing these light curves for measurement of transit properties such as the transit depth, transit duration, and planet-to-star radius ratio. The transit depth is measured to be  $1.063 \pm 0.070\%$ , the transit duration to be  $0.894 \pm 0.0013$  days, and a corresponding planet-to-star ratio of  $0.1031 \pm 0.0034$  was determined. These values are compared to those in [Bakos et al. \(2011\)](#) and [Sada & Ramón-Fox \(2016\)](#) and found to be of similar value.

## 1. INTRODUCTION

The first exoplanets to ever be detected were discovered in 1992 by radio astronomers Aleksander Wolszczan and Dale Frail (Wolszczan & Frail 1992). This discovery brought with it a new realm of observational astronomy that has caused our understanding of planetary evolution and behavior to grow exponentially. Transit detection, a technique that emerged over the course of exoplanet study, has resulted in the the discovery of hundreds of exoplanets within the past twenty years. This technique has transcended professional astronomers and has become achievable for amateur astronomers to perform as well. This project will take an amateur approach to exoplanet transit detection using the equipment provided at the Mt. Stony Brook Observatory in Stony Brook, NY.

When viewing an exoplanetary system, the planet periodically eclipses the host star. Observations from the eclipsing period, or transit, can provide astronomers a variety of information not measurable by other means alone. This includes atmospheric composition of the planet and the relative dimensions of planet and host star. Additionally, other measurements such as the dynamical mass from the Doppler planet-detection method can be used in conjunction with transit measurements to determine the planet's density and internal composition. This study will focus on one result of exoplanet transit observation by comparing the flux drop of the host star during transit. When the exoplanet passes in front of the host star, light is blocked such that the observed flux is measured as,

$$\Delta F/F \approx \left(\frac{R_p}{R_\star}\right)^2 \quad (1)$$

Where  $F$  is the flux, and  $R_p$  and  $R_\star$  are the radii of the planet and host star, respectively. As evident, the change in flux is proportionate to the ratio  $\frac{R_p}{R_\star}$ . We expect to measure this ratio, as well as the transit depth and duration from our flux measurements. All calculated values will be compared to known values found in other literature.

HAT-P-23b is a ...

## 2. OBSERVATIONS

### 2.1. *Finding the Target*

The first step of our observations was finding our target exoplanetary system for our study. This began by downloading a series of primary transit exoplanets from the online exoplanet catalog.<sup>1</sup>. Our target was to find an exoplanetary system observable from Stony Brook, NY, around the nights of September 9th, 2019 at about 10:00 PM EST.

For each potential candidate we found the hour angle  $HA$  as

$$HA = LST - \alpha \quad (2)$$

Where LST is the Local Sidereal time for Stony Brook NY at  $319.5^\circ$ , and  $\alpha$  is the right ascension (RA) of each of our potential system candidates. We narrowed our list down by keeping candidates

<sup>1</sup> [http://exoplanet.eu/catalog/all\\_fields/](http://exoplanet.eu/catalog/all_fields/)

with an hour angle of  $0 \pm 3$  degrees. The declination  $\delta$  of our candidates was also considered. Stony Brook, NY is located at a latitude of about  $41^\circ$ . The declination range of acceptable targets were calculated as:

$$90^\circ - 41^\circ = 49^\circ \quad (3)$$

For a range of  $[-49^\circ:90^\circ]$ . For each remaining candidate that fell within the declination range, transit depth was calculated as:

$$\delta_T = \left( \frac{R_p}{R_\star} \right)^2 \quad (4)$$

Where radii values were taken from the exoplanet catalog. Transit depths were compared to the stellar magnitudes of each host star where we isolated stars with magnitudes bright enough to be seen with our equipment. Our magnitude constraint was stars less than about 12 due to pollution in the area. Our final calculation was for the transit duration  $T_D$  of each candidate. If an exoplanet began its transit at the planet's edge, it would be  $b$  above/below the horizontal centerline of the planet, and distance  $l$  away from the vertical centerline of the planet, creating a right triangle with hypotenuse  $R_p + R_\star$  where  $l$  is defined as:

$$l = \sqrt{(R_p + R_\star)^2 + b^2} \quad (5)$$

where  $b = 0$  since we assume the exoplanet transits through the center of the star. Since this is only halfway across, we must double the value of  $l$  get a final transit distance of

$$d = 2l = \sqrt{(R_p + R_\star)^2} \quad (6)$$

$$d = R_p + R_\star \quad (7)$$

We know that the total transit duration must be some fraction of the orbital period  $P$  for the star-planet system. As the exoplanet goes along the orbit during transit it follows a linear distance of  $2l$ , or  $d$ , equating to angle  $\theta$  in the exoplanet orbit. The angle can be found through simple trigonometric reduction as,

$$\sin \frac{\theta}{2} = \frac{l}{a} \quad (8)$$

$$\theta = \arcsin \frac{d}{a} = \arcsin \frac{(R_p + R_\star)}{a} \quad (9)$$

where  $a$  is the semimajor axis. Therefore, if the duration of transit is a fraction of the orbital period  $P$  by the orbital distance  $\theta$  crossed during transit, we get our final equation,

$$T_{dur} = P \theta \pi^{-1} = \frac{P}{\pi} \arcsin \left( \frac{R_\star + R_p}{a} \right) \quad (10)$$

With all values accessible from the exoplanet catalog. This is an 'upper limit' measurement since an exoplanet would have the longest transit duration at a star's center, as there would be the greatest distance of star for an exoplanet to have to cross. Any transit at a higher or lower inclination would have much less of the star to pass by, making for a shorter transit duration. In our calculations, we considered the exoplanet to be crossing at the star's center, therefore making it an upper limit to the

real duration. Transit duration was calculated for each remaining candidate. Our candidates were restricted further to have a transit duration between one to three hours for a one-night observation.

Our final target was HAT-P-23b with coordinates 20 24 29.72 +16 45 43.81. Exoplanet transit was calculated to occur on the night of September 18th, 2019 with ingress at 21:35:54 EST, transit midpoint at 22:56:36 EST, and egress at 00:17:18 EST. This equates to a transit duration of 2.69 hours and an estimated transit depth of 1.193%.

## 2.2. *Instrumentation*

Our observations used the Mt. Stony Brook observatory with the 14-inch Meade LX200-ACF telescope on a Mesu-200 German Equatorial Mount with 900 arcmin field-of-view. We attached the 1024x1024 SBIG STL-1001E CCD camera under *R*-filter operated with the CCDSoft software. This camera was cooled to 0° to minimize the effect of dark current. Table 1. provides a general summary of our observations. Additionally, we set our CCD to 1x1 binning, with exposure times chosen to avoid CCD saturation with an average count about 65e3 per pixel.

We began taking our science images at 00:39:55.72 UTC, about an hour and a half before ingress time. At the time 02:30:03.398 UTC, we paused our observations to perform a meridian flip as our target crossed the meridian. We resumed our observations at 02:44:03.595 UTC and completed observations at 04:54:42.43 UTC, about twenty minutes after our expected egress. Images were taken with a 60-second exposure for a total of 277 science images. Standard procedures were used to calibrate CCD images. This included taking a series of ten 60-second dark exposures and a series of ten 2-second dome flats, with the dome flat's exposure time adjusted as to not saturate the images. For all of our images with the exception of our dome flats, AutoDark reduction was not applied.

**Table 1.** Summary of Photometric Observations on the Night of 9/18/19

Instrument	Object	Filter	Exposure Time (s)	Observation Start (UTC)	Observation End (UTC)	No. Images	Weather
Meade 14"/SBIG STL-1001e	HAT-P-23b	<i>R</i>	60	2019-09-19 00:39:55.572	2019-09-19 04:54:42.437	227	Clear
Meade 14"/SBIG STL-1001e	Dome Flats	<i>R</i>	2	2019-09-19 05:08:32.575	2019-09-19 05:09:31.202	10	Clear
Meade 14"/SBIG STL-1001e	Dark Frames	<i>R</i>	60	2019-09-19 05:10:47.233	2019-09-19 05:20:36.026	10	Clear

## 3. DATA REDUCTION

### 3.1. *Image Calibration*

We median-combine our both our series of 10 dark frames and 10 dark-corrected dome flats to create a master dark and master flat frame respectively. To correct for CCD sensitivity and dark current, we subtract the master dark and divide by the master flat for each of our science images using the `pyraf`<sup>2</sup> software. Fig. 1 provides an example of our image correction for one of our science images.

Hot pixels that are easily saturated and dead pixels that receive no photons exist in all of our images. These 'bad' pixels can affect our measurements and make our flux values inaccurate. To

<sup>2</sup> [www.stsci.edu/institute/software\\_hardware/pyraf](http://www.stsci.edu/institute/software_hardware/pyraf)

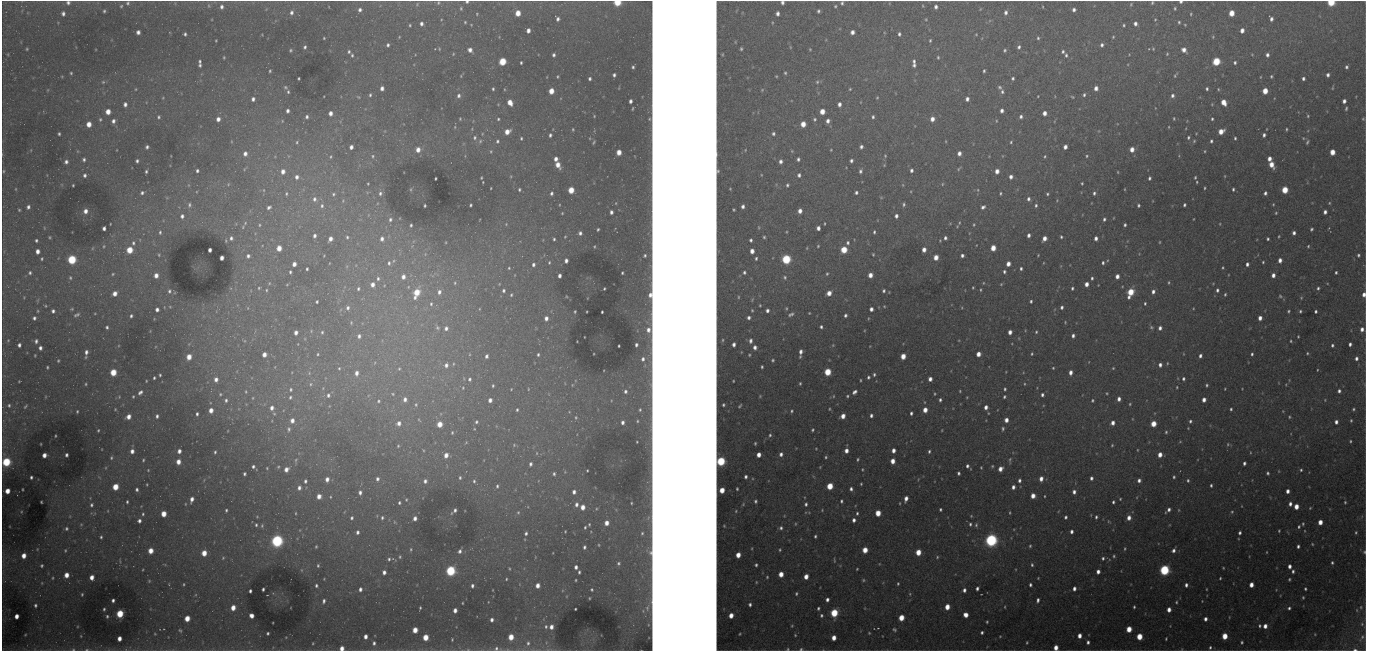


**Figure 1.** Examples of corrected single science image (right) against uncorrected image (left). On the uncorrected image, donuts and vignetting are present. The effects are visibly reduced on the corrected image.

correct for this quality, we create a bad pixel map that identifies hot and dead pixels. The bad pixels are the outliers in the count distribution of our two master frames. We define our outlying values to be  $\pm 4\sigma$  (standard deviations) from the mean of each master frame. Fig. 2 exemplifies the affect of the 4-sigma clip on the master dark frame where 0.084% of pixels were rejected as hot pixel outliers.

From the figure, we can see the 4-sigma clip is a valid choice of cutoff. Fig. 3 depicts the distribution of counts for the master flat with the same cutoff, rejecting about 0.1% of all pixels as hot pixels. The locations of all the dead pixels were found and mapped on the same image (Fig. 4). We applied this map by passing it to SExtractor, which corrected for bad pixels that may offset our later measurements of flux.

### 3.2. Aperture Photometry on Target and Calibration Stars

Calibrated images were solved for their World Coordinate System (WCS) transformations using the `solve-field` method from Astrometry.net<sup>3</sup> and the Stony Brook University Astrolab machines. Each science image was then processed through the Source Extractor<sup>4</sup> on the same machines with an aperture of 8.137 pixels. The aperture was measured as the radius of a fitted region around our host star in the SAOimage ds9 software<sup>5</sup>. From the images, 10 reference stars were chosen of similar brightness. These calibration stars will be used to correct for relative variations in our lightcurve. The coordinates of each reference star can be seen in Table 2.

<sup>3</sup> <http://astrometry.net/doc/readme.html>

<sup>4</sup> <http://www.astromatic.net/software/sextarator>

<sup>5</sup> <http://ds9.si.edu/site/Home.html>

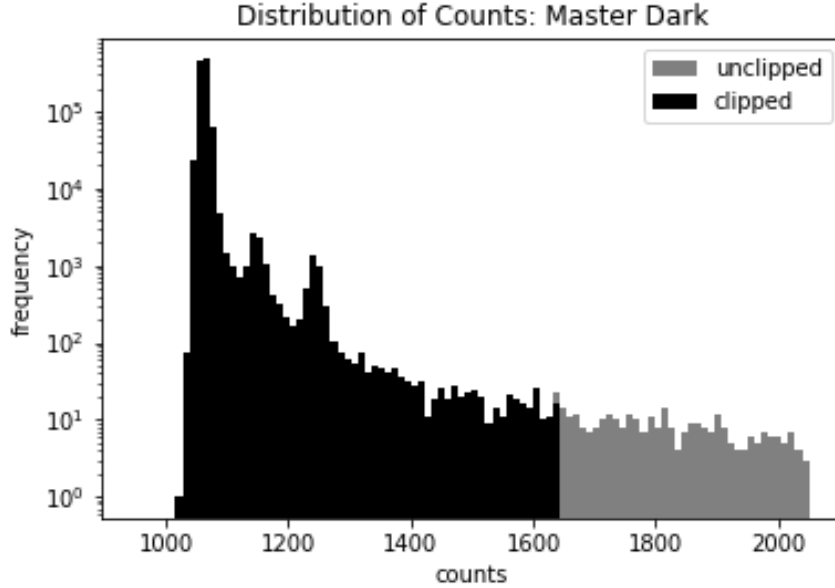


**Figure 2.** Histogram of distribution of 4-sigma clipped counts for master dark frame in log-y scale.

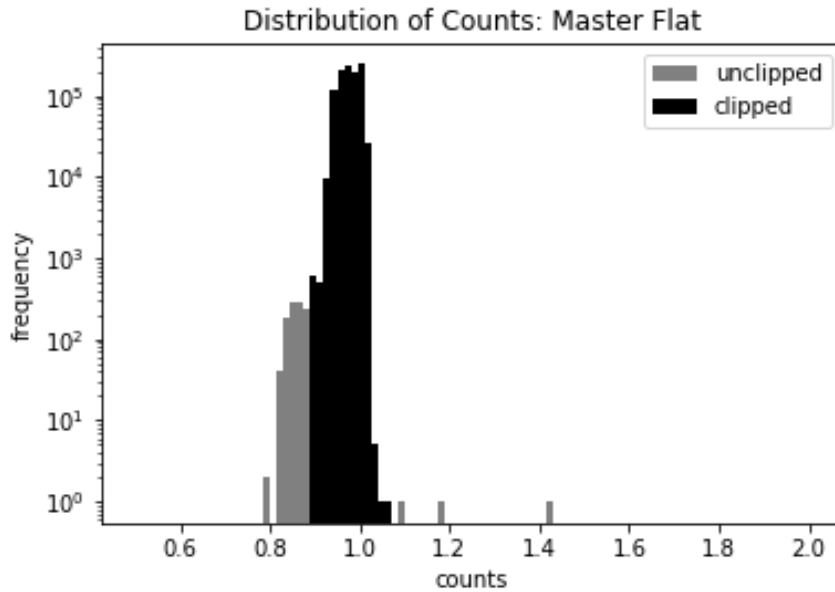


**Figure 3.** Histogram of distribution of 4-sigma clipped counts for dark-corrected master flat frame in log-y scale.

For each reference star  $j$ , we re-scaled both the flux and error on the flux for their images:

$$f_j(t) \rightarrow \frac{f_j(t)}{\langle f_j \rangle} \quad (11)$$

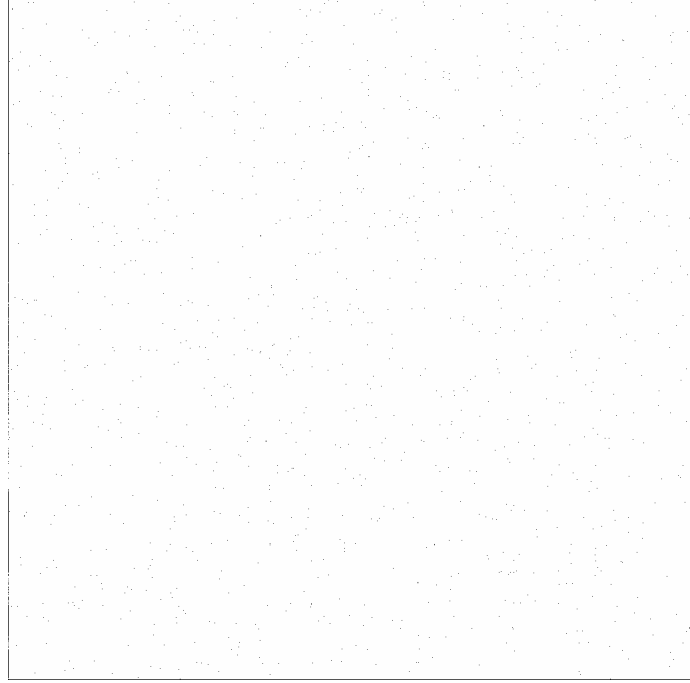


**Figure 4.** Bad pixel map sample with bad pixels labeled in black.

**Table 2.** Coordinates for Calibration Stars

No.	RA ( $\alpha$ )	DEC ( $\delta$ )
1.	306.1064114	16.7437909
2.	306.1520304	16.7849426
3.	306.173349	16.7745184
4.	306.117797	16.7007637
5.	306.150734	16.8051701
6.	306.0601808	16.7604594
7.	306.1666074	16.7072902
8.	306.2072257	16.7279283
9.	306.0954369	16.7998087
10.	306.0439028	16.6929899

$$\sigma_{f_j(t)} \rightarrow \frac{\sigma_{f_j(t)}}{\langle f_j \rangle} \quad (12)$$

Where  $f_j$  is the flux of the  $j$ th reference star exposure, and  $\langle f_j \rangle$  is the average flux value for all  $j$ th reference star exposures. This will help us to visualize the relative variations due to changes in airmass, the atmosphere, and intrinsic variations of stellar brightness. In Fig. 5, we plot our initial

**Table 3.** Sample summary of science image flux and error, weighted mean and error of all reference stars, and ratio and error values

Time Obs.	$f_{\text{sci}}$	$\sigma_{f_{\text{sci}}}$	$\mu_i^{\text{ref}}$	$\sigma_i^{\text{ref}}$	$r_i$	$\sigma_{r_i}$
00:44:14.699	102346.80	294.95220	0.99573	0.00109	102785.64	316.86058
00:45:19.496	103146.10	297.61010	0.98961	0.00110	104228.75	322.14182
00:46:24.262	102172.00	298.73710	0.98270	0.00110	103970.26	325.63439
00:47:29.075	103665.10	304.30020	0.99867	0.00112	103803.20	326.33947
00:48:33.873	105406.80	294.07480	1.00967	0.00108	104397.79	311.97426
00:49:38.655	104860.10	294.13580	1.00649	0.00108	104184.27	312.97245
00:50:43.436	103526.70	294.14570	0.99775	0.00108	103760.55	315.63298
00:51:48.202	104715.50	294.05120	1.00294	0.00108	104409.06	314.04694
00:52:53.001	104359.40	293.18500	1.01132	0.00108	103191.42	310.22260
00:53:57.783	104778.60	293.71740	1.00440	0.00108	104319.39	313.19591
00:55:02.533	103891.90	293.04830	1.00343	0.00108	103537.04	312.57797
00:56:07.283	105005.60	293.45240	1.00815	0.00108	104157.06	311.71265
00:57:12.018	104511.00	293.38700	0.99986	0.00108	104525.14	314.34328
00:58:16.768	104986.20	293.65520	1.00671	0.00108	104286.76	312.39010
00:59:21.566	103269.80	291.96720	0.99160	0.00108	104144.15	315.38797
01:00:26.332	104209.50	292.78830	1.00628	0.00108	103558.74	311.44146
01:01:31.113	105659.20	293.66840	1.01604	0.00108	103991.06	309.44899
01:02:35.895	105429.10	293.00420	1.01724	0.00108	103641.90	308.36722
01:03:40.676	106035.30	294.14620	1.01629	0.00108	104335.83	310.01128

lightcurve for our host star.

All ten reference lightcurves were also plotted on the same graph, such that each reference star was offset by a small value (Fig. 6). Across all lightcurves there is a drop in flux toward the middle and a few individual exposures whose fluxes are significantly lower than the others. We remove these outlying exposures from our image by defining an exposure cutoff of any scaled flux less than 0.98. Applying this cutoff to one reference star will indicate which exposures have this variation. Since the variations are consistent across all stars, we know those exposures had the same affect on all stars. Therefore, once we locate the outlying exposures, we remove them from all our stars.

This cutoff led to a total of 25 exposures to be removed from our data. The removal of these exposures allows for a better idea about the shape of the stellar lightcurves. The re-scaled lightcurves of the calibration stars can be seen in Fig. 7. While the outlying exposure frames were removed, changes in atmospheric conditions caused flux changes that were larger than the signal we were

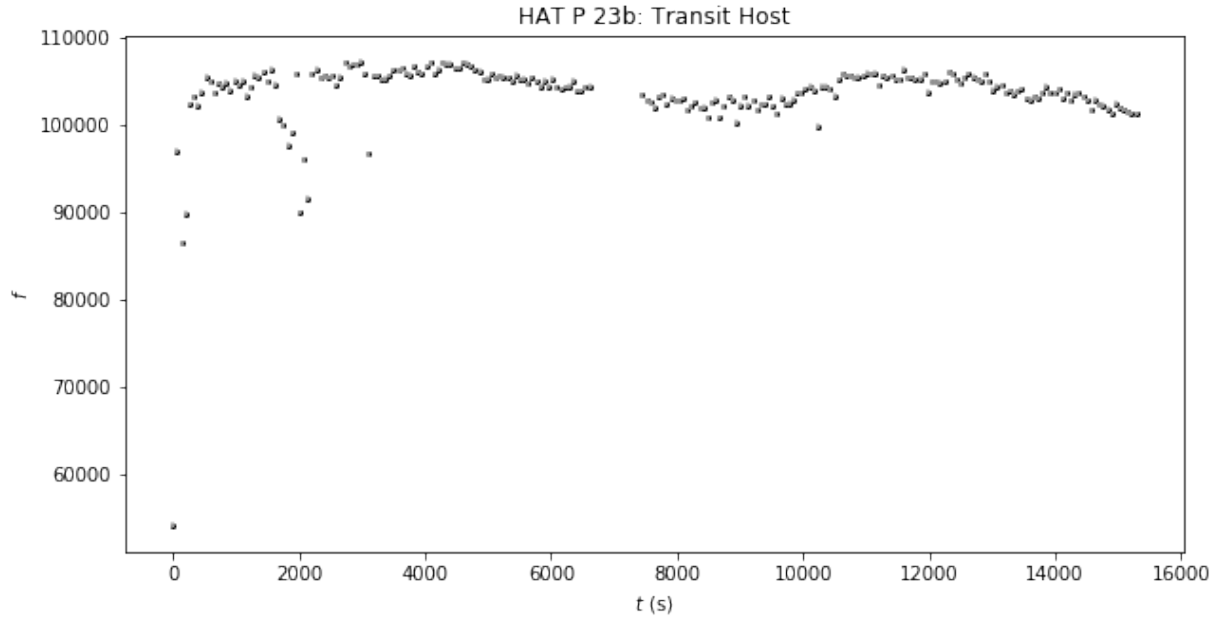


**Figure 5.** Lightcurve for HAT-P-23b of flux against time since observation. Plot is of unscaled flux against time since observation start in seconds.

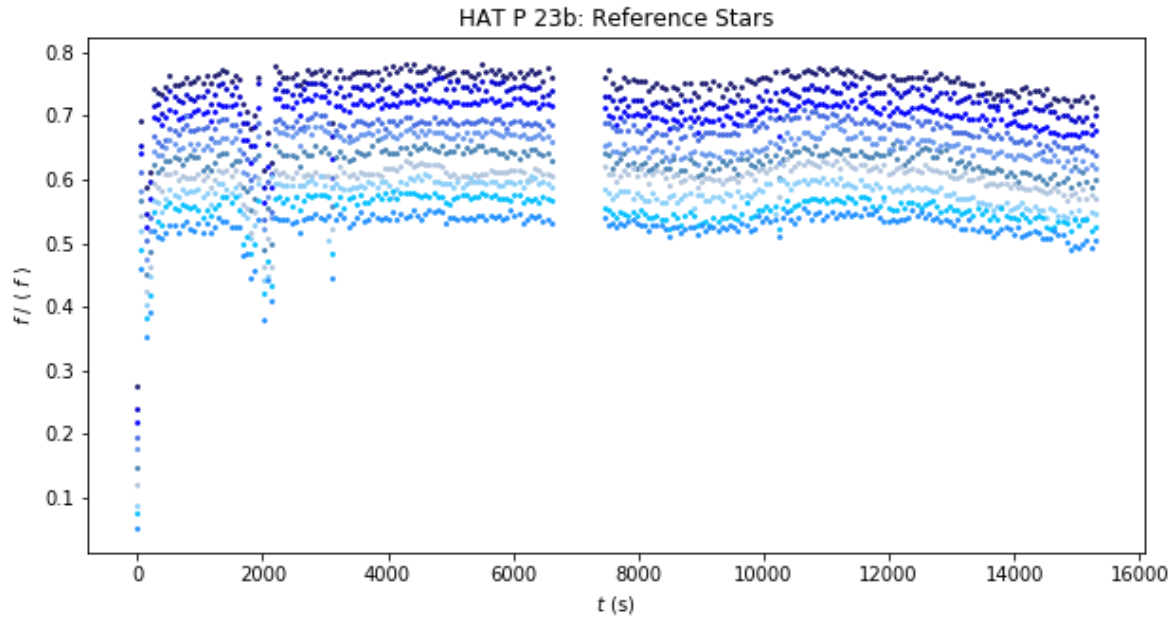


**Figure 6.** Initial lightcurve for 10 calibration stars with scaled flux. Plot is of scaled flux against time since observation start in seconds.

trying to detect. The effect of this is a visual dip in our flux values towards the middle of every light

curve. As with our outlying exposures, we must correct for this to accurately see the host star transit.

We now calculate flux of the target stars relative to the reference stars to account for these atmospheric changes. By averaging over several reference stars, we can reduce the statistical noise as well as systematic uncertainty from undetected variability in the reference stars. When computing the average flux of several stars, we compute the weighted mean:

$$\mu_i^{\text{ref}} = \frac{\sum f_j^{\text{ref}} / (\sigma_j^{\text{ref}})^2}{\sum 1 / (\sigma_j^{\text{ref}})^2} \quad (13)$$

as well as its error:

$$\sigma_i^{\text{ref}} = \sqrt{\frac{1}{\sum_j 1 / (\sigma_j^{\text{ref}})^2}} \quad (14)$$

Here we sum all fluxes from ten reference stars at the  $i$ th exposure, Where  $f_j^{\text{ref}}$  is the flux at the

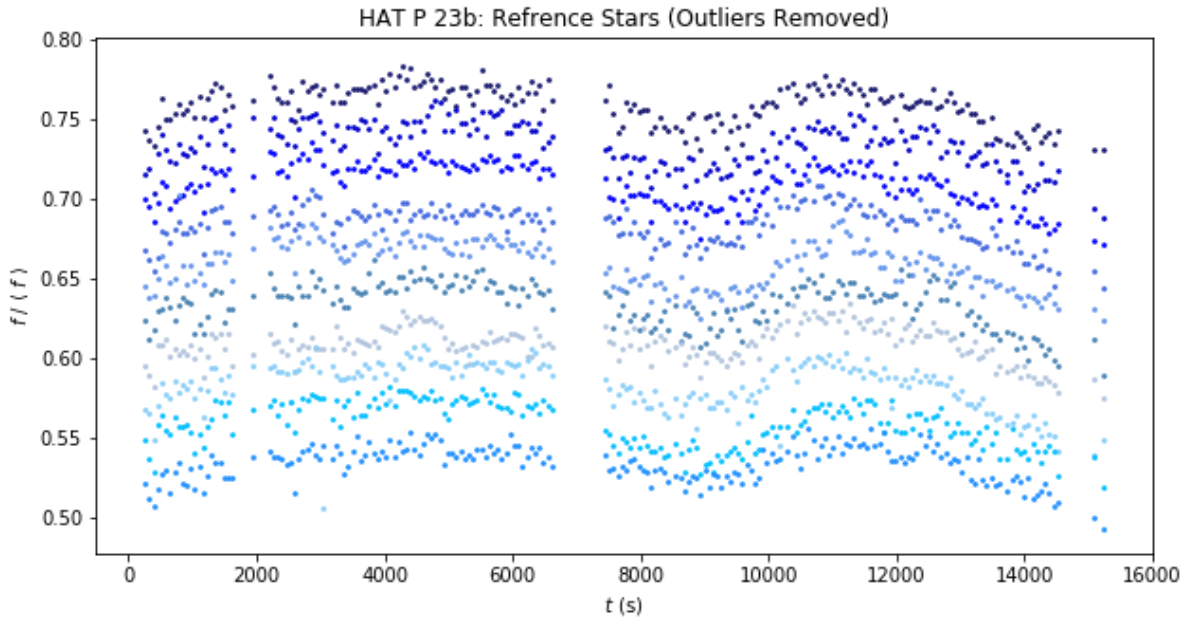


**Figure 7.** Lightcurves for 10 reference stars with removed outliers for scaled flux against time since observation start.

$i$ th exposure frame. We additionally define the ratio  $r_i$  as:

$$r_i = \frac{f_i^{\text{sci}}}{\mu_i^{\text{ref}}} \quad (15)$$

and its error:

$$\sigma_{r_i} = r_i \sqrt{\left( \frac{\sigma_i^{\text{ref}}}{\mu_i^{\text{ref}}} \right)^2 + \left( \frac{\sigma_{f_i}}{f_i} \right)^2} \quad (16)$$

The new ratio values are plotted against time since observation start in Fig. 7, where we can see a more distinct lightcurve. For each image  $i$ , the flux of the science image  $f_i^{\text{sci}}$  and its error, the weighted mean  $\mu_i^{\text{sci}}$  and its error, and the ratio  $r_i$  and its error in were saved a separate text file. A sample of this data is seen in Table 3.

We now plot the vertical lines to mark the transit ingress, midpoint, and egress to get an idea if these values are valid on our lightcurve. The updated lightcurve can be seen in Fig. 9.

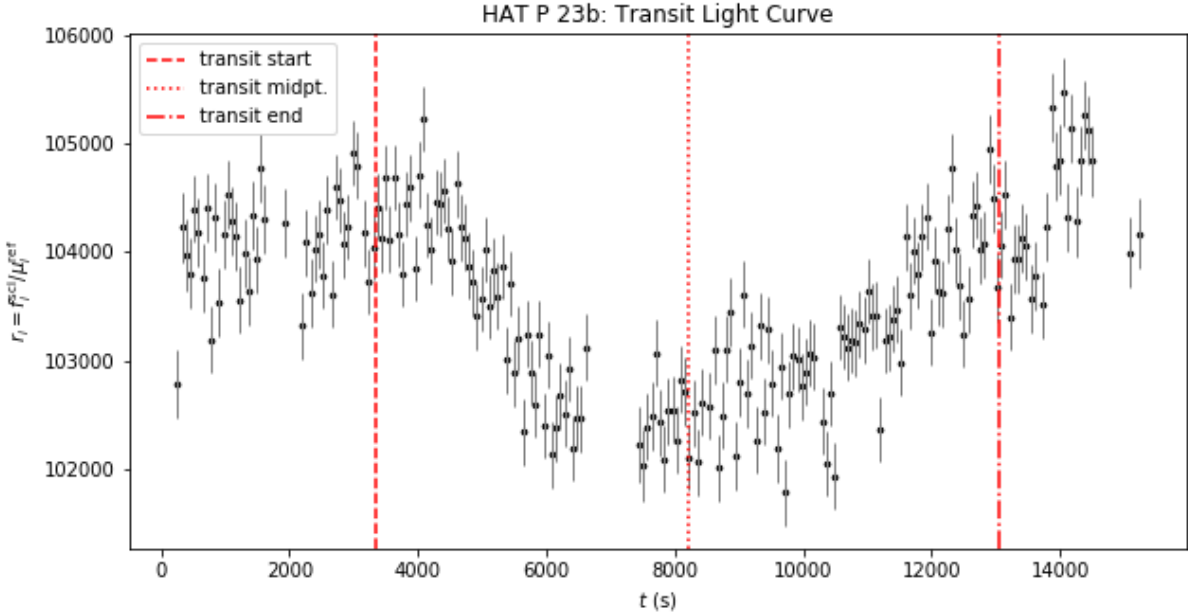


**Figure 8.** Lightcurve for HAT-P-23b with transit expected time points marked, with ratio  $r$  and seconds  $t$  since observation start.

As evidenced in the figure, our expected times do not seem to match up with our lightcurve. We visually estimate our transit to start at about 980 seconds passed our expected time with an error of about 120 seconds. A new egress time is also calculated by using the difference of the adjusted ingress time to the mid-transit time and adding that value to the mid-transit time, such that:

$$t_e = (t_m - t_i) + t_m \quad (17)$$

Where  $t_e$  is the egress time,  $t_m$  the mid-transit time, and  $t_i$  is the adjusted ingress time. As the mid-transit line is in what appears to be the middle of the transit, we do not adjust this measurement. The adjusted transit times are again plotted along the lightcurve in Fig. 10.

The adjust transit times are much better fitted to the lightcurve. Our new transit begins at 21:51:54 EST and ends at 00:33:18 EST. We calculate a new transit duration of  $T_D = 7724.0 \pm 120$  s, or  $T_D = 0.0894 \pm 0.00139$  days, about thirty minutes shorter than our expected duration.

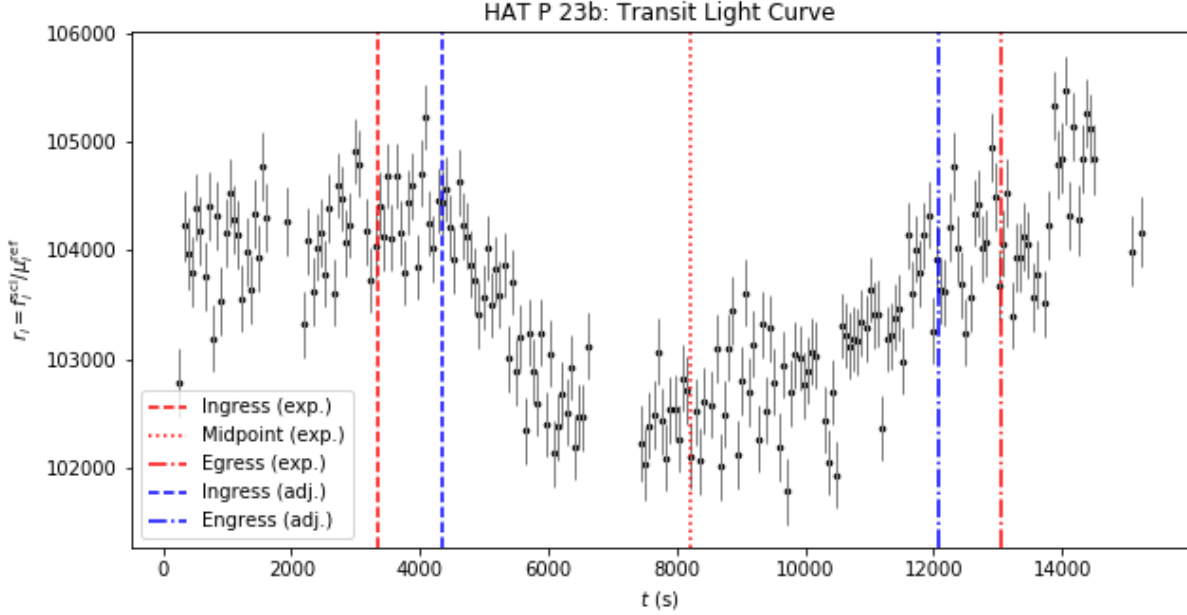


**Figure 9.** Lightcurve for HAT-P-23b with transit expected and adjusted time points marked, with ratio  $r$  and seconds  $t$  since observation start.

With the adjusted transit ingress and egress time it is possible to calculate transit depth,  $\delta_T$ . The baseline flux  $f_B$  of our image is calculated as the mean of ratio flux measurements before ingress. We divide our ratios by this value to normalize our data and calculate the error:

$$\sigma_{r_{n,i}} = r_{n,i} \sqrt{\left(\frac{\sigma_{ri}}{r_i}\right)^2 + \left(\frac{\sigma_{fB}}{f_B}\right)^2} \quad (18)$$

Where  $r_{n,i}$  is the normalized ratio values. The ratio  $r_B$  now represents the fraction of light from our science target that is not obscured by the transiting planet and we get a new normalized lightcurve (Fig 11). For the normalized lightcurve, we expect the behavior:

$$r_B - \epsilon = r_T \quad (19)$$

Where  $\epsilon$  is a constant, and  $r_T$  is the ratio during transit. Before and after the eclipse, ratio  $r_B$  should scatter around 1.0 and drop a value of  $1.0 - \epsilon$  during the eclipse. We calculate our  $r_B$  value by binning our data and using the unweighted mean in the bin of the normalized ratio values before ingress. The mean and weighted mean of the ratio values during transit are also calculated for the value  $r_T$ . We found  $r_B = 1.00081 \pm 0.00057$ ,  $r_T = 0.99018 \pm 0.0004$  for an epsilon value of  $\epsilon = 0.01063 \pm 0.0007$  equating to a transit depth of  $\delta_T = 1.063 \pm 0.070\%$

#### 4. DISCUSSION

Before and after transit, the host star's flux seems about consistent. There is a bit more variation after egress, however the baseline flux was calculated using only the values before transit. In regards

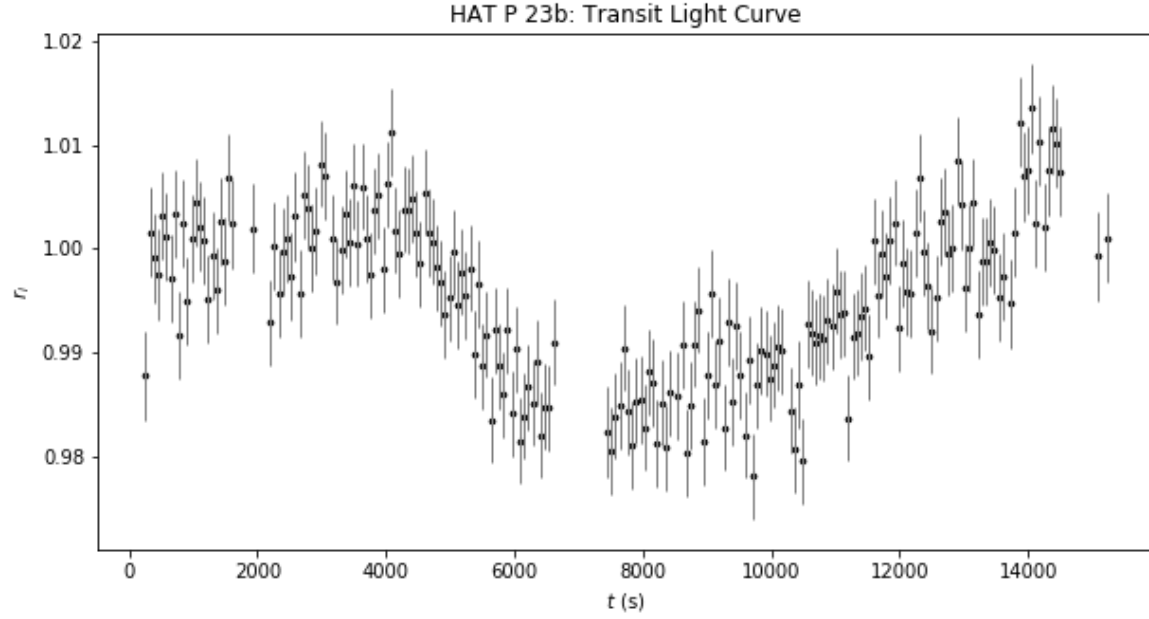


**Figure 10.** Lightcurve for HAT-P-23b with normalized ratio  $r_i$  and seconds  $t$  since observation start.

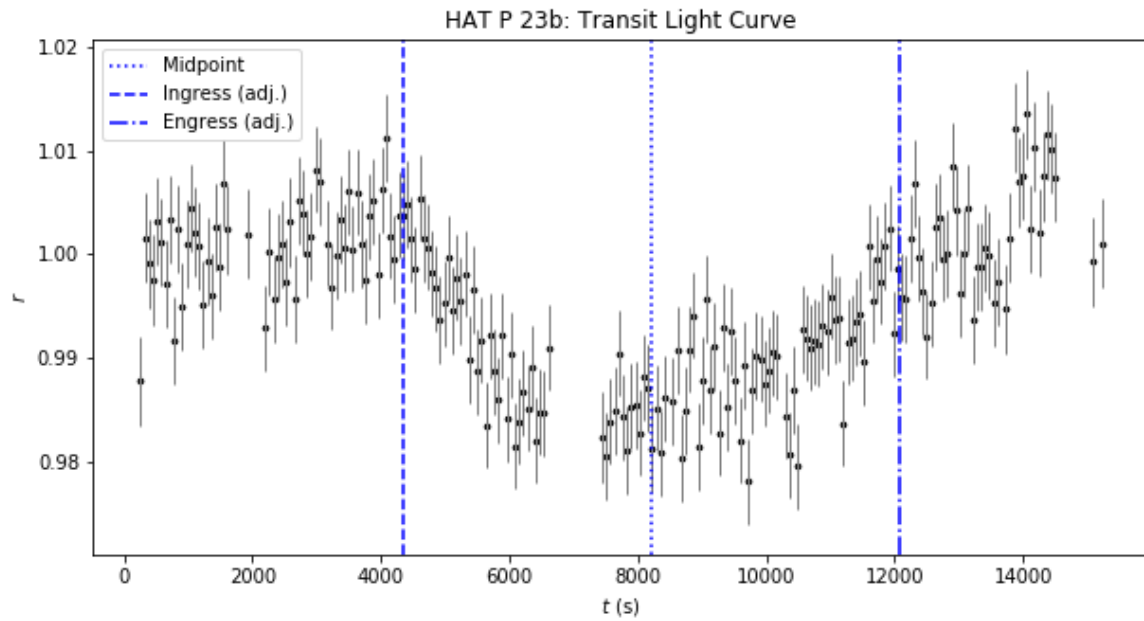


**Figure 11.** Final lightcurve for HAT-P-23b with transit time points marked, with normalized ratio  $r$  and seconds  $t$  since observation start.

to the actual lightcurve itself, we see there is a distinct dip during the transit time. As expected, this was measured to be about a 1% decrease in stellar flux and is visually detectable (Fig. 12).

Compared to our expected measurement of  $f = 1.193\%$ , our value for transit depth is a bit under the value; However, [Bakos et al. \(2011\)](#) has found HAT-P-23b to have a transit depth of  $1.04\%$ . This value is quite similar to ours and falls within our range of error of  $\pm 0.07\%$

With our transit depth, we can estimate our planet-to-star radius ratio  $R_p/R_\star$  as:

$$\frac{R_p}{R_\star} = \sqrt{\epsilon} \quad (20)$$

where

$$\sigma_{\frac{R_p}{R_\star}} = \frac{\sigma_\epsilon}{2\sqrt{\epsilon}} \quad (21)$$

Where we get our value for  $R_p/R_\star$  to be  $0.1141 \pm 0.0012$ . Table 4. presents a summary of our ratio values compared to two studies, [Bakos et al. \(2011\)](#) and [Sada & Ramón-Fox \(2016\)](#). Compared to their measurements, we find our value of the planet-to-star ratio to be in agreement, with a significance around  $1\sigma$ .

Our measurements are valid in comparison to literature values, however they are not exact. For studies such as [Bakos et al. \(2011\)](#), multiple transits of HAT-P-23b were observed. The future work of this study may benefit by following similar methods and incorporating more observations of the transit. Multiple transit observations allow for more data and therefore more definite measurements for our system. Similarly, we could approach this study through the lens of a telescope at a location of much less light pollution. It is expected that this would allow for more precise observations with less atmospheric effects. This study also consisted of only a small amount of measurements, whereas other studies found more quantities. Increasing the amount of measurements could additionally help estimate our ability to measure exoplanetary system qualities.

**Table 4.** Coordinates for Calibration Stars

	$T_d$ (days)	$\delta_T$ (%)	$R_p/R_\star$
This Work	$0.0894 \pm 0.00139$	$1.063 \pm 0.070$	$0.1031 \pm 0.0034$
Bakos et al. (2011)	$0.0908 \pm 0.0007$	1.047	$0.1169 \pm 0.0012$
Sada & Ramon-Fox (2016)			$0.1113 \pm 0.001$

## 5. CONCLUSION

From this study we were able to learn the extent at which we are able to use amateur equipment for exoplanet transit measurements. Our final lightcurve model presented a clear dip during our exoplanet eclipse, with a slight difference in expected ingress and egress (Fig. 12). The transit depth is measured to be  $1.063 \pm 0.070\%$ , the transit duration to be  $0.0894 \pm 0.0013$  days, and a corresponding planet-to-star ratio of  $0.1031 \pm 0.0034$  was determined. All of our values were a few sigma to measurements of other studies (Table 4). This is indicative of the abilities of Mt. Stony Brook to be acceptable for these types of measurements.

## REFERENCES

- Bakos, G. Á., Hartman, J., Torres, G., et al. 2011, ApJ, 742, 116, doi: [10.1088/0004-637X/742/2/116](https://doi.org/10.1088/0004-637X/742/2/116)
- Sada, P. V., & Ramón-Fox, F. G. 2016, PASP, 128, 024402, doi: [10.1088/1538-3873/128/960/024402](https://doi.org/10.1088/1538-3873/128/960/024402)
- Wolszczan, A., & Frail, D. A. 1992, Nature, 355, 145, doi: [10.1038/355145a0](https://doi.org/10.1038/355145a0)